

# Photomultiplier Short-Term Stability for Radiation Detection

Leonardo F. M. C. C. Ribeiro

May 2020

## 1 Introduction

Photomultiplier tubes (PMTs) are detector devices used to capture light signals and are of vital importance in radiation detection and spectroscopy. They are useful for both direct detection of photons as well as coupling to other detector materials. For example, PMTs can be used in conjunction with scintillator materials<sup>1</sup> to transform their light output into a more desirable electrical signal. Correctly understanding and characterizing PMT behavior is crucial if one is to obtain accurate experimental data from them.

Several experiments have been carried out in order to assess various PMT characteristics such as efficiency, linearity of response, and resistance to external conditions [1, 2]. This work focuses on what happens at the initial stages of PMT operation following the introduction of a bias voltage and current in the anode. This is usually called the warm-up period, and PMT response can drift during this time. Manufacturers recommend warming up a PMT before taking data for up to 60 minutes [3, 4].

The Bay Area Neutron Group (BANG) at the University of California, Berkeley and Lawrence Berkeley National Laboratory uses Hamamatsu PMTs for radiation detection and neutron time-of-flight measurements [5]. Data from Hamamatsu suggests its PMT model R6095 may have its output reduced to 95% of its initial value over 1000 minutes of warming up [3]. Evidently, this could pose an issue for radiation detection experiments, especially those requiring high precision and steady response. However, PMT stability varies greatly by model and this data cannot be directly extrapolated to the PMTs used by BANG. The main objective of this report is to examine the stability of the H1949-51 model PMT during warm-up.

One particular application of interest is Compton edge characterization, which is used by BANG for light output calibration (see Section 3). PMT drift directly affects the detector gain and resolution, resulting in movement of the position of the Compton edge. This work will capitalize on these movements as an indication of PMT drift.

---

<sup>1</sup>Scintillators are materials that luminesce when struck by ionizing radiation.

The following two sections provide relevant background information on the functioning of PMTs, the mechanism of drift, and the Compton edge characterization method. The subsequent sections explore the data analysis methodology and the experimental design and results, with data showing H1949-51 stability at different bias voltages.

## 2 Technical Description of PMTs

An extensive description of PMTs in the context of radiation detection is given by Knoll [6]. PMTs are coupled to scintillators, collecting their light as input. They make use of the external photoelectric effect to amplify incoming light pulses and transform them into electrical signals that can be read by digital or analog data acquisition systems. The main components of a PMT (which can be seen in Fig. 1) are a photocathode, several dynodes, and an anode, all residing inside a vacuum tube with a window [3]. To better understand its functioning, the amplification process may be broken down into three parts.

### 2.1 Photoelectron Emission

Incoming scintillation light enters the vacuum tube through a transparent window. Several materials are employed in PMT windows, which select against certain wavelengths based on their transmission coefficients. The H1949-51 has a borosilicate glass window. It transmits radiation with wavelengths no shorter than 300 nm (ultraviolet range) [3].

The transmitted photons hit the photocathode, triggering the photoelectric effect. The minimum photon energy required to eject an electron with this mechanism is the material’s work function. However, there are several energy loss mechanisms for the electron in its trajectory toward the surface of the material. Therefore, the ejection of electrons is a statistical process that depends on the energy transferred to them and the height of the potential barrier [6]. The ratio of incident photons to ejected electrons is called the quantum efficiency of the cathode. The H1949-51 photocathode has a quantum efficiency of about 25% for wavelengths between 200 and 450 nm [3].

The most common photocathodes are semiconductor films with low work functions [3], where electrons do not have to travel long before finding a boundary and do not require much energy to overcome the ejection barrier. The H1949-51’s photocathode is made of a mixture of two alkali alloys: Sb-Rb-Cs and Sb-K-Cs. This is often referred to as a “bialkali” photocathode. In addition, this is a transmission type photocathode: electrons are ejected in the same direction as the photon flux, on the opposite side of the photocathode film [7].

### 2.2 Amplification

At this point, the photocathode has transformed the scintillator light signal into an electrical current. The current passes through a focusing electrode with an

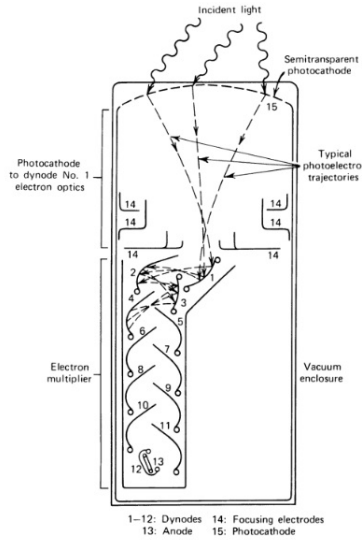


Figure 1: Basic Structure of a Photomultiplier Tube (From Radiation Detection and Measurements. [6])

aperture that acts as a collimator until it hits the first of a series of dynodes, also known as secondary emissive electrodes [3]. In each of these stages, incoming electrons hit the dynode and excite secondary electrons. An electric field is maintained between the photocathode and the first dynode, and between any two consecutive dynodes. This causes secondary electrons to accelerate and ensures they strike the next dynode with more energy than they had when emitted. As a result, the number of emitted electrons increases with each stage of the process [3].

The current multiplication induced by interaction with one dynode is called the secondary emission ratio ( $\delta$ ) and it depends strongly on the accelerating voltages [3]. The total gain is defined as the current amplification provided by the entire dynode chain. Intuitively, for a sequence of  $n$  dynodes with the same value of  $\delta$ , the gain is:

$$\mu = \delta^n. \quad (1)$$

There are several possible arrangements for a dynode chain, such as circular, continuous or linear [3]. The H1949-51 model has 12 dynode stages organized in a linear-focused fashion<sup>2</sup>.

### 2.3 Collection

When the amplified electron current reaches the end of the dynode chain, it is large enough to be collected and serve as a readable electrical signal. An

<sup>2</sup>See Figure 1 for an example of linear-focused dynode chain.

anode collects the electrons coming from the last dynode and the signal can be forwarded to data acquisition systems.

## 2.4 Drifting

PMT instability can be divided into variations observable over the long term (e.g., aging, fatigue) and the short term (i.e., drift or stress). Long term gain fluctuations are attributable to photocathode and dynode degradation. Excessive illumination may trigger thermal diffusion, inducing irreversible microstructural evolution and surface depletion in the plates, especially those coated with cesium [8]. In addition, secondary electrons may ionize any residual gas in the tube. The heavy ions accelerate and hit the dynodes, causing irreparable damage [8]. As a result, PMTs close to the end of their lifetime suffer fatigue. In addition, manufacturers recommend aging new PMTs—essentially warming up, but for dozens of hours—before this initial drift stabilizes and a PMT can be employed in high precision experiments [3, 4]. The H1949-51 PMT studied in this work had been used for several years and multiple high current experiments prior to the work described in this report. Furthermore, the time scale for long term variations is much larger than the duration of the experiments. There is no reason to expect aging or fatigue to play an important role in its instability.

PMT drift is thought to be predominantly attributable to variations in the secondary emission ratio [3]. External factors such as ambient pressure, magnetic fields, and electric fields can affect the PMT response significantly [9]. However, the systematic decrease in PMT response during warm-up is attributable to voltage hysteresis effects [3, 9]. When the supply voltage changes abruptly (i.e., a stepwise function), a feedback loop within the internal PMT circuitry may cause the output to overshoot and slowly return to its original level [3]. Biasing an unbiased PMT represents a significant step change. A schematic is shown in Figure 2.

It is also possible for a PMT to suffer hysteresis when the input light changes abruptly. It has the same effects as voltage hysteresis, although the latter is expected to be much more significant [3].

## 3 Compton Edge Characterization

In order to investigate the PMT response during warm-up, a source was placed incident on the detector and successive light output calibrations were performed as a function of time using Compton edge characterization.

In a Compton scattering interaction, a photon interacts with an electron in the medium, transferring part of its energy. The electron gains momentum and moves at an angle relative to the initial photon direction. By conservation of energy and momentum, the photon changes its direction by an angle  $\theta$  and its frequency by a function of the angle [10]. The simple kinematics of this process

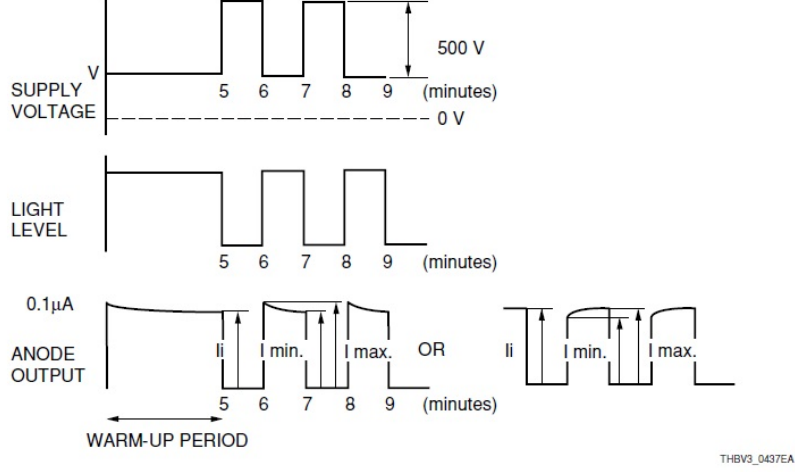


Figure 2: Procedure used by Hamamatsu to measure voltage hysteresis effects in a PMT of unknown model. The top plot shows the voltage being changed abruptly and periodically. The middle plot shows the illumination conditions (cycling light levels induce the ideal circuit behavior in order for voltage hysteresis to happen). The bottom plot shows the hysteresis effects on the anode output at  $0.1 \mu\text{A}$ . [3]

enables one to write the energy shift of a given recoil photon as:

$$E' = \frac{E}{1 + \frac{E(1 - \cos \theta)}{mc^2}}. \quad (2)$$

Here  $E$  is the incident photon energy;  $E'$  is the scattered photon energy;  $m$  is the electron rest mass;  $c$  is the speed of light in vacuum; and  $\theta$  is the angle between the direction of the incident photon and the direction of the scattered photon.

This expression reaches a minimum when the cosine term is equal to -1, implying the existence of a maximum energy for the recoil electron occurring at a scattering angle of  $\pi$  radians. By conservation of momentum, this electron would move in the same direction as the incident photon. If a distribution of recoil electrons is obtained for a material being irradiated with monoenergetic  $\gamma$  rays interacting mainly through Compton scattering, one would expect there to be a maximum recoil electron energy. This is called the Compton edge.

Cs-137 emits a prominent  $\gamma$  line at 662 keV, with the Compton edge at 478 keV. These photons interact with the scintillator detector primarily through Compton scattering. The recoil electrons excite molecules in the scintillator, which emit visible light upon de-excitation [6]. The scintillation light output is related to the recoil electron energy through the electron light yield relation, which increases monotonically as a function of electron energy. The proportionality of this light yield is a topic of active research [11, 12]. In this work light

output calibrations are relative, so there is no need to take into account any non-proportionality. The scintillation light can then be measured by a PMT, and the Compton edge feature can be studied by making histograms of the PMT pulse amplitude.

The expected shape of a recoil energy distribution is given by the Klein-Nishina (KN) equation<sup>3</sup>. The KN distribution predicts a sharp cutoff at the Compton edge. However, real data show a smeared edge feature. One reason for this is the possibility of double scattering in the material, which defies one of the underlying assumptions behind the KN formula. The most significant reason for a spread, however, is the resolution of the detector. Dietze and Klein [13] relate the shape of a pulse signal to three independent resolution parameters according to the following relation:

$$\Delta L/L = \sqrt{\alpha^2 + \beta^2/L + \gamma^2/L^2}. \quad (3)$$

Here  $L$  is the integrated signal;  $\Delta L$  is the full width at half maximum (FWHM) of the signal;  $\alpha$  represents the locus dependent collection at the photocathode;  $\beta$  represents the statistical nature of all mechanisms involved (Compton scattering, attenuation, photoelectric effect, electron multiplication in PMT); and  $\gamma$  represents the electronic noise from the PMT and all other circuits.

The resolution function depends on detector geometry, efficiency of light transport and collection by the PMT, and inhomogeneities in the photocathode [14] and can be estimated theoretically or experimentally [13].

Additionally, one can define a linear detector light output function:

$$E_e = aL + b. \quad (4)$$

Here  $E_e$  is the energy of a recoil electron;  $a$  and  $b$  are experimental quantities describing the response of the detector.

If a detector is assumed to behave according to these two expressions, a calibration consists of finding the parameters that best describe the detector response. This can be done by modeling the detector's response to a monoenergetic  $\gamma$  source whose Compton edge position is known, taking real data with this source, and matching the model to experimental data by varying the parameters described above. For more details on the implementation of the calibration method used in this work, see Section 5.

Figure 3 shows that despite the described spread, the Compton edge region is still clearly recognizable in the pulse amplitude histogram. It appears as a prominent shoulder after which the counts decrease dramatically (as indicated by the black data points).

PMT drift affects the response of the detector. If one takes data during PMT warm-up, the measured Compton edge may drift over time as a result. Assuming the H1949-51 has a resolution of the form described in Equations 3 and 4, and assuming all parameters are independent, gain drift results in a

---

<sup>3</sup>The Klein-Nishina equation gives the cross section for Compton interactions described by Equation 2. It is derived under a single hit assumption for incoming photons.

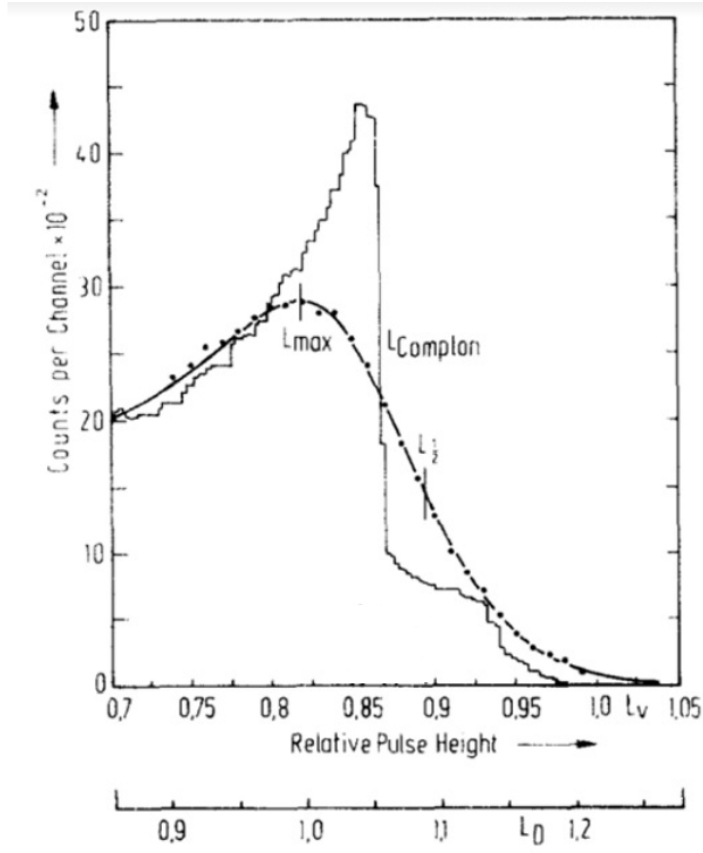


Figure 3: Pulse height histograms from a Na-22 source (adapted) [13]. The curve with the highest peak is a Monte Carlo simulation; the isolated points represent real data. The continuous smeared curve represents the simulation after it's been transformed with the resolution and response parameters to fit the experimental data (this process is called folding). The light units are relative.

change in the  $a$  parameter. Observing the variations in  $a$  as a function of time during PMT warm-up will be a useful way to describe drift while maintaining the context of detector calibration applications.

## 4 Experiment Setup

One H1949-51 PMT was optically coupled to an EJ-309 liquid organic scintillator contained in a thin aluminum housing with BC-630 silicone grease. The PMT was biased using a CAEN R1470ET high voltage power supply. A CAEN V1730 500 MS/s digitizer module read the PMT output voltage every 2 ns,

triggering freely upon detection of a signal above a threshold. A  $10\text{ }\mu\text{Ci }^{137}\text{Cs}$  source was placed about 15 cm away from the detector (see Figure 4). At this distance, the scintillator was illuminated in a sufficiently uniform manner. If one places the source too close to the scintillator, the recoil electron distribution may become biased as a result of non-uniform photon incidence. This effect becomes significant when the distance between source and scintillator drops below one scintillator length—in this case, approximately 5 cm.

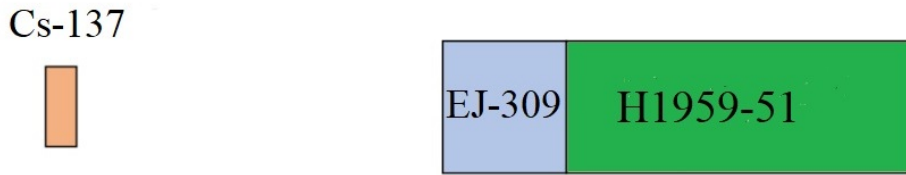


Figure 4: Schematic of experimental setup.

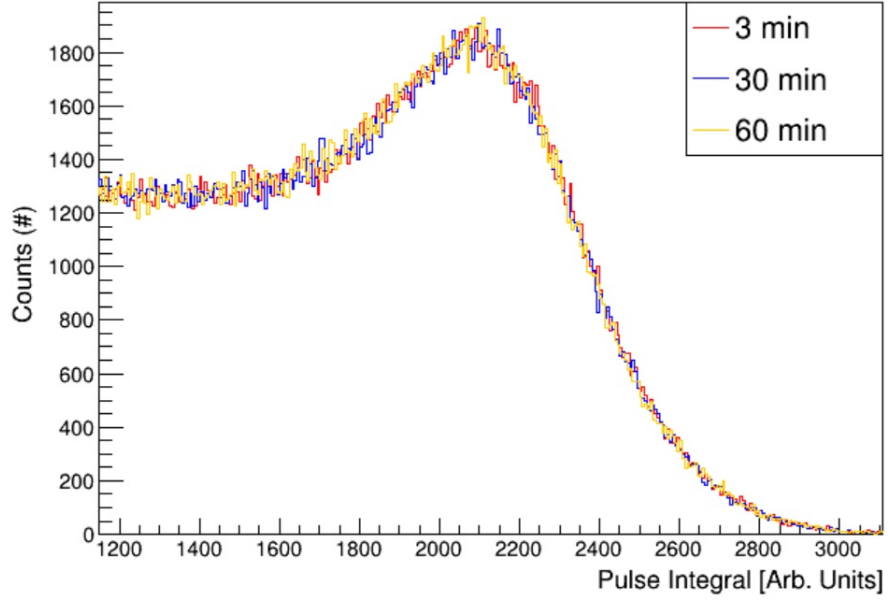
The bias voltage and data acquisition are turned on at the same time to study the behavior of the PMT as it warms up. Two data sets were taken using the same PMT with two different bias voltages (1300 V, 1700 V), and with a cool-down period of several days between runs. The data rate was different between experiments as a result of the differing gains. Due to the fixed, 200 MB output file size of the data acquisition system, the amount of time corresponding to a single run was also different between experiments. In total, the 1300 V runs took 85 minutes, or about 4 minutes per file; the 1700 V runs took 175 minutes, or about 7 minutes per file.

## 5 Data Analysis

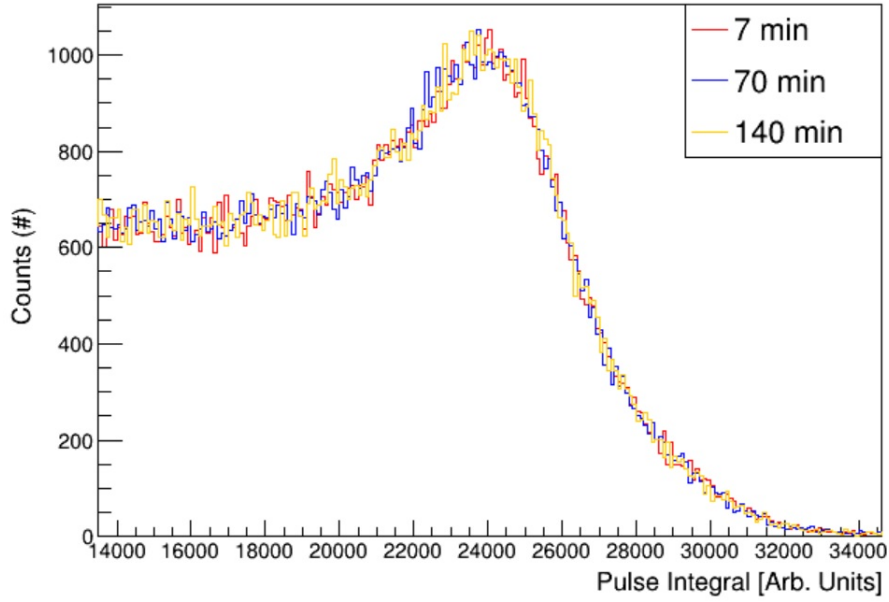
The raw traces were integrated with an integration length of 300 ns and used to generate pulse integral histograms. Figure 5 presents uncalibrated histograms from both data sets showing the Compton edge feature at various times during each experiment. The histograms are close to each other and any movement in the position of the edge cannot be discerned by the naked eye. As discussed in Section 3, calibrating these histograms can provide a better understanding of the relative position of the edges.

Calibration was done by comparing the measured pulse integral histograms with a Monte Carlo simulated  $^{137}\text{Cs}$  energy deposition spectrum created with the GEANT4 software [15]. The simulation yields more accurate predictions than using the Klein-Nishina formula because it incorporates the effects of  $\gamma$ -ray double scattering in the scintillator. The synthetic data was modified by





(a) 1300 V.



(b) 1700 V.

Figure 5: Uncalibrated pulse integral histograms showing Compton edges from data taken near the start, middle, and end of experiments.

the five parameters described in Eqs. 3 and 4 and by a simple scalar parameter that multiplies the entire histogram to account for the size of the data set. In addition, two more parameters were introduced to model background with a power-law distribution. The mean squared error between real and synthetic data is then minimized with a  $\chi^2$  minimization that takes these eight parameters as its variables.

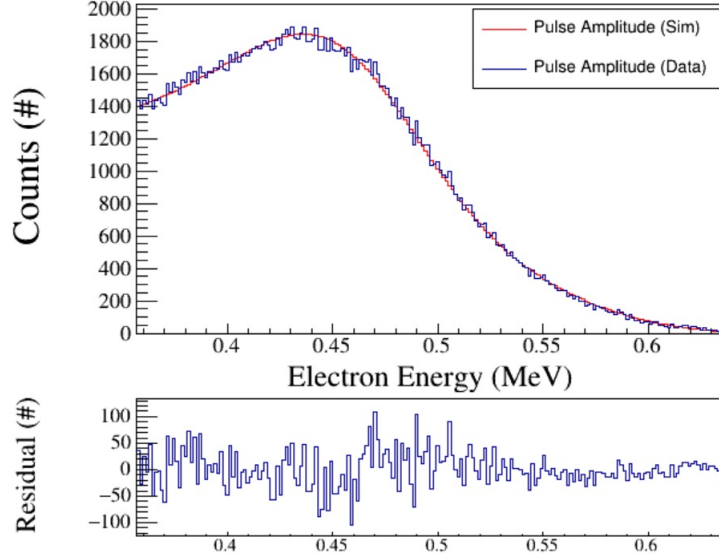
## 6 Results

Figure 6 shows two spectra calibrated with and without the power-law background, respectively. The residual plots represent the error in each bin reflecting the goodness of the fit, and these plots indicate that accounting for background results in smaller and more steady error in the Compton edge region. One can also see that the Compton edge position is not accounted for accurately unless the background parameters are included. All subsequent calibrations mentioned in this report included a power-law background for higher accuracy.

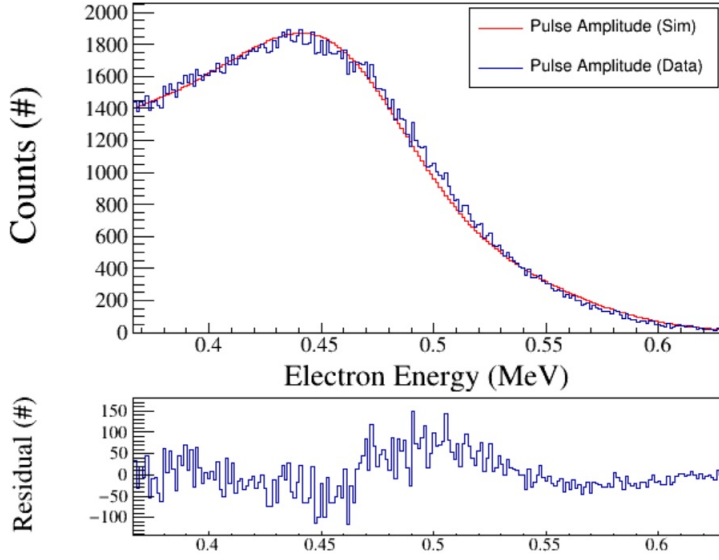
The first data file for each data set (1300 V and 1700 V) was calibrated according to the procedures discussed above, generating 8 fit parameters for each. For the other data files, seven out of eight parameters were fixed at the values given by the first calibration. Only the  $a$  parameter (see Eq. 4) was allowed to vary and contribute to the minimization. Since only one parameter varies from fit to fit, tracking this parameter over time can potentially reveal PMT gain drift. Figure 7 shows the calibration fit performed on the first file of the 1700 V data set.

Figure 8 shows the variation of the  $a$  parameter as a function of time for both the 1300 V (blue) and 1700 V (magenta) data sets. In both sets, the variations stay well below 1%, indicating negligible drift influence in the time intervals considered.

A prominent feature is a variance increase at later runs. This may be due to variations in other resolution parameters, which were assumed to stay constant for this analysis. Furthermore, the lack of PMT drift did not change significantly with an increase in the bias voltage.



(a) With background



(b) Without background

Figure 6: Calibration fits performed with data taken at 1300 V with and without including the power-law background. In both cases, the Compton edge feature was isolated and the simulated spectrum (red) was fit to the experimental data (blue) using the detector response parameters described in the text. The residual plot shows the difference between both curves after fitting for each case.

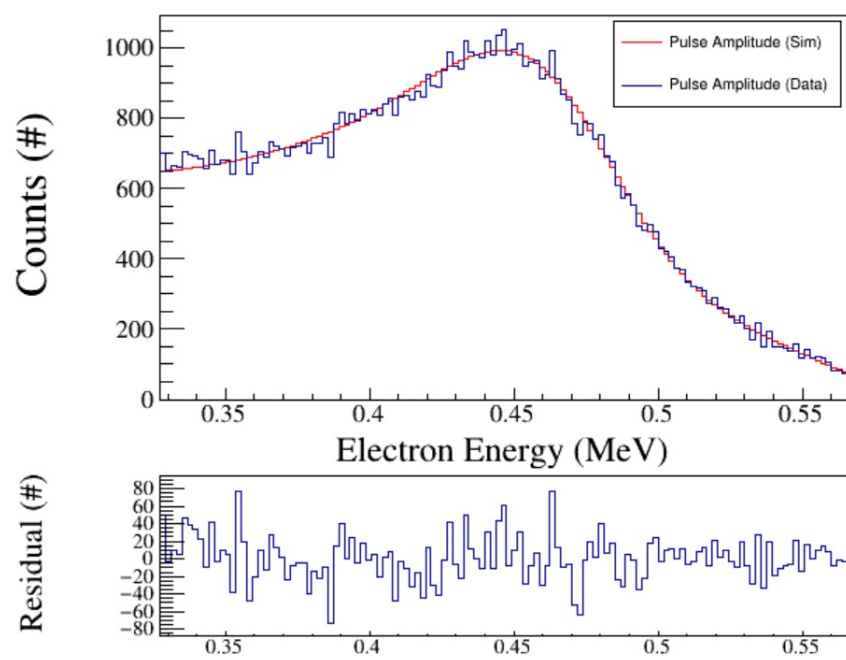


Figure 7: Example of calibration fit performed in the first file of the 1700 V data set.

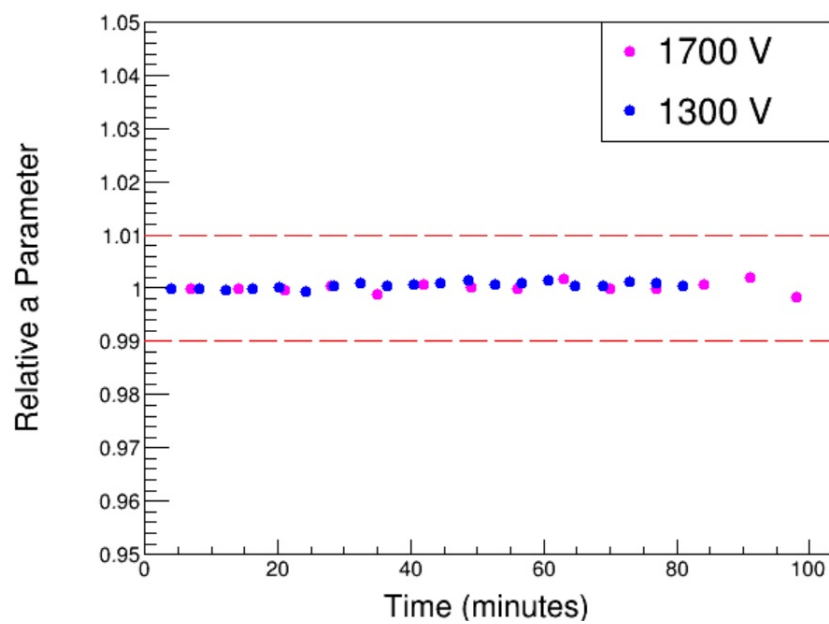


Figure 8: Variation in the  $a$  parameter with time for both data sets. Values are given relative to the first parameter. For both data sets, the time at 0 minutes corresponds to the initial application of a bias voltage, as well as the start of the data acquisition. The red lines indicate 1% boundaries. Note the zero-suppressed ordinate axis.

## 7 Conclusion

The data obtained in this experiment suggests that gain drift during warm-up in the Hamamatsu H1949-51 PMT is small (well within 1%) with biases of 1300 V or 1700 V. However, this is insufficient evidence to neglect the impact of warm-up on PMT experiments. Due to the experimental limitations described below, additional work is necessary to provide deeper insight into PMT warm-up behavior. Any future work should aim to address these limitations.

Firstly and most importantly, the  $^{137}\text{Cs}$  source used in this experiment was relatively weak (10  $\mu\text{Ci}$ ). PMT instability is known to increase with anode current [3]. For this reason, a statement of work has been prepared at Lawrence Berkeley National Laboratory to enable use of a much stronger  $^{137}\text{Cs}$  source (5 mCi) for future experiments of this sort. The anode current induced by the 5 mCi source is more similar to that seen in many in-beam neutron detection experiments performed by BANG.

Additionally, this work was limited to one PMT with two bias voltages. Data must be taken at several different voltages before characterizing the dependence of drift on gain. Characterizing multiple PMTs of the same model can show whether PMT warm-up behavior varies from PMT to PMT.

Finally, this analysis fixes all calibration fit parameters except for  $a$  under the assumption that this is the only parameter subject to warm-up. It is possible that some of the other parameters change with time during warm-up. This would make the analysis more complicated than simply tracking the magnitude of the  $a$  parameter.

In spite of these limitations, the methods employed in this report constitute a promising way of measuring PMT drift via Compton edge characterization. Future work within BANG will seek to continue this characterization effort in order to enable more precise nuclear science experiments.

## References

- [1] Michael P. Bristow, Donald H. Bundy, and Anthony G. Wright. Signal linearity, gain stability, and gating in photomultipliers: application to differential absorption lidars. *Appl. Opt.*, 34(21):4437–4452, Jul 1995.
- [2] P. Dorenbos, J. T. M. de Haas, R. Visser, C. W. E. van Eijk, and R. W. Hollander. Absolute light yield measurements on  $\text{BaF}_2$  crystals and the quantum efficiency of several photomultiplier tubes. In *IEEE Conference on Nuclear Science Symposium and Medical Imaging*, pages 257–259 vol.1, 1992.
- [3] Hamamatsu Photonics. *Photomultiplier tubes: basics and applications*, 3rd edition, 2007.
- [4] Photonis. *Photomultiplier tubes: Principle and Applications*, 2002.

- [5] K.P. Harrig, B.L. Goldblum, J.A. Brown, D.L. Bleuel, L.A. Bernstein, J. Bevins, M. Harasty, T.A. Laplace, and E.F. Matthews. Neutron spectroscopy for pulsed beams with frame overlap using a double time-of-flight technique. *Nuclear Instruments and Methods in Physics Research Section A: Accelerators, Spectrometers, Detectors and Associated Equipment*, 877:359 – 366, 2018.
- [6] Glenn F. Knoll. *Radiation Detection and Measurement*, pages 275–320. John Wiley and Sons, Inc., 4th edition, 2010.
- [7] Photomultiplier tube assembly H1949-51 specifications, online. <https://www.hamamatsu.com/eu/en/product/type/H1949-51/index.html> (accessed May 1, 2020).
- [8] S. Donati. *Wiley Encyclopedia of Biomedical Engineering*, chapter Photomultipliers. John Wiley and Sons, Inc., 2006.
- [9] M.S. Zucker. An improved method for the stabilization of NaI-photomultiplier gamma detectors against thermal and other drift. *Nuclear Instruments and Methods in Physics Research Section A: Accelerators, Spectrometers, Detectors and Associated Equipment*, 242(2):306 – 314, 1986.
- [10] James E. Turner. *Atoms, Radiation, and Radiation Protection*, pages 177–185. John Wiley and Sons, Inc., 3rd edition, 2007.
- [11] J. J. Manfredi, B. L. Goldblum, T. A. Laplace, G. Gabella, J. Gordon, A. O’Brien, S. Chowdhury, J. A. Brown, and E. Brubaker. Proton light yield of fast plastic scintillators for neutron imaging. *IEEE Transactions on Nuclear Science*, 67(2):434–442, Feb 2020.
- [12] T. A. Laplace, B. L. Goldblum, J. A. Brown, D. L. Bleuel, C. A. Brand, G. Gabella, T. Jordan, C. Moore, N. Munshi, Z. W. Sweger, A. Sweet, and E. Brubaker. Low energy light yield of fast plastic scintillators. *Nuclear Instruments and Methods in Physics Research. Section A, Accelerators, Spectrometers, Detectors and Associated Equipment*, 954, 10 2018.
- [13] G. Dietze and H. Klein. Gamma-calibration of NE 213 scintillation counters. *Nuclear Instruments and Methods in Physics Research*, 193(3):549 – 556, 1982.
- [14] Horst Schölermann and Horst Klein. Optimizing the energy resolution of scintillation counters at high energies. *Nuclear Instruments and Methods*, 169(1):25 – 31, 1980.
- [15] S. Agostinelli, J. Allison, K. Amako, J. Apostolakis, H. Araujo, P. Arce, M. Asai, D. Axen, S. Banerjee, G. Barrand, et al. Geant4 – a simulation toolkit. *Nuclear Instruments and Methods in Physics Research Section A: Accelerators, Spectrometers, Detectors and Associated Equipment*, 506(3):250 – 303, 2003.